



# The deep oxidation of NO was realized by Sr multi-site doped $\text{g-C}_3\text{N}_4$ via photocatalytic method

Meng Zhou<sup>a</sup>, Guohui Dong<sup>a,\*</sup>, Fangke Yu<sup>a,\*</sup>, Yu Huang<sup>b</sup>

<sup>a</sup> School of Environmental Science and Engineering, Shaanxi University of Science and Technology, Xi'an, 710021, China

<sup>b</sup> Key Laboratory of Aerosol Chemistry and Physics, Institute of Earth Environment, Chinese Academy of Sciences, Xi'an, 710061, China



## ARTICLE INFO

### Keywords:

Photocatalysis  
NO removal  
 $\text{g-C}_3\text{N}_4$   
Sr doping  
Multi-site doping

## ABSTRACT

The NO removal activity of  $\text{g-C}_3\text{N}_4$  is limited by many shortcomings including the high recombination rate of photo-generated carriers and secondary pollution induced by incomplete oxidation. Here, we modified  $\text{g-C}_3\text{N}_4$  using multi-site Sr-doping with simultaneous N atoms replacement, cavity padding, and intercalation. The NO removal experiments showed that multi-site doping of Sr improved the NO removal rate by 1.5 times. Meanwhile, the conversion rate of secondary pollution ( $\text{NO}_2$ ) decreased from 62.5% to 15.8%. The effects of doped Sr were different with different doping modes. All the doping modal of Sr could decrease the band gap of  $\text{g-C}_3\text{N}_4$ . Meanwhile, the Sr that intercalated in the interlayer of  $\text{g-C}_3\text{N}_4$  could improve the transfer of photo-generated electrons; the Sr that replaced the N atoms could help the activation of  $\text{O}_2$  to produce more  $\cdot\text{O}_2^-$ ; the Sr padded in the cavity provides  $\text{g-C}_3\text{N}_4$  with the ability to activate the  $\text{H}_2\text{O}_2$  for the generation of a stronger oxidant ( $\cdot\text{OH}$ ). The different doping modes complement each other and combine to realize efficient and deep NO removal.

## 1. Introduction

With the increasingly serious environmental pollution, air pollution is an urgent problem because it has a great impact on the environment and also greatly harms human health [1]. Among the various air pollution problems, NO emissions are one of the most serious problems because NO is a cause of acid rain, haze, photochemical smog, and ozone depletion [2]. Some traditional methods such as selective catalytic reduction (SCR) and selective non-catalytic reduction (SNCR) can effectively resolve high concentrations (ca. 800 ppm) of NO pollution in factory chimneys, but they are not viable when purifying low concentrations (ca. 600 ppb) of NO in some human settlements (such as garages) [3–5]. Moreover, the costs of traditional technologies are expensive because they require high operating temperatures and precious metals. Compared with traditional methods, photocatalytic technology is more suitable for the purification of low concentrations of NO [6,7]. This is because low concentrations of NO reside in sunshine or lamp-light, and sunshine and lamplight are the energy sources for photocatalytic technology. Moreover, photocatalytic technology is a low cost, easily operated and eco-friendly technology [8].

Among the variety of photocatalysts,  $\text{g-C}_3\text{N}_4$  is a promising photocatalyst for NO removal because of three features. First, it has a suitable band width (2.7 eV) and can remove NO under visible light irradiation [9–13]. Second, it can be synthesized by the calcination of carbon and nitrogen-rich substances, such as melamine, urea, thiourea, etc., which results in very low costs for  $\text{g-C}_3\text{N}_4$  [14]. Third, it is a steady metal-free polymer photocatalyst, and thus it cannot release metal ions that threaten our environment [15]. However, previous reports indicate that the performance of  $\text{g-C}_3\text{N}_4$  is not high enough. The poor NO removal performance is due to two aspects: one is that the NO removal rate is low, and the other is the incomplete oxidation of NO (the product contains a large amount of  $\text{NO}_2$ ) [16]. The low removal rate is because the separation and migration efficiency of the photogenerated carriers are relatively low, which may be caused by the stratified structure of  $\text{g-C}_3\text{N}_4$  because the electron transfer between two adjacent layers is difficult. The incomplete oxidation may relate to the surface atom structure of  $\text{g-C}_3\text{N}_4$ . Although  $\text{O}_2$  can be activated to oxide species such as  $\cdot\text{O}_2^-$  and  $\text{H}_2\text{O}_2$  on the surface of  $\text{g-C}_3\text{N}_4$ , the  $\text{H}_2\text{O}_2$  is difficult to be further activated to the stronger oxide species ( $\cdot\text{OH}$ ) [17]. Therefore, the  $\text{g-C}_3\text{N}_4$  system has difficulty producing the strong oxide species

**Abbreviations:** CNSrx, different amounts of Sr modified  $\text{g-C}_3\text{N}_4$  ( $x = 0.025, 0.05, 0.075$ ); XRD, X-ray diffraction; XPS, X-ray photoelectron spectroscopy; UV-vis, ultraviolet-visible; UV-vis DRS, ultraviolet-visible diffuse reflectance spectrometry; EPR, electron paramagnetic resonance; SEM, scanning electron microscopy; PL, photoluminescence; EIS, electrochemical impedance spectroscopy; DFT, density functional theory; PDOS, partial density of states

\* Corresponding authors.

E-mail addresses: [dongguohui@sust.edu.cn](mailto:dongguohui@sust.edu.cn) (G. Dong), [yufangke@sust.edu.cn](mailto:yufangke@sust.edu.cn) (F. Yu).

<https://doi.org/10.1016/j.apcatb.2019.117825>

Received 9 January 2019; Received in revised form 27 May 2019; Accepted 5 June 2019

Available online 06 June 2019

0926-3373/© 2019 Elsevier B.V. All rights reserved.

(·OH) for the exhaustive oxidation of NO. Therefore, to efficiently and thoroughly remove NO, the modification method should consider the above two aspects. In the past few years, many modification methods such as metal or non-metal doping, molecular copolymerization, and the construction of heterojunctions have been developed to improve the photocatalytic performance of g-C<sub>3</sub>N<sub>4</sub> [18]. However, these methods do not consider the electron transfer between two adjacent layers and the effect of the surface atom structure on the generation of reactive oxygen species.

Recently, Dong's research group reported that the intercalation of Sr could form a charge channel between two adjacent layers, thereby improving the charge transfer efficiency and enhancing the photocatalytic NO removal activity [19]. It is a pity that they did not consider the modification of the surface structure. In our previous report, the Sr terminal helped in the activation of O<sub>2</sub> and H<sub>2</sub>O<sub>2</sub> [20]. Therefore, we speculate that the introduction of Sr in both the interlayer and surface of g-C<sub>3</sub>N<sub>4</sub> will significantly improve the photocatalytic NO removal of g-C<sub>3</sub>N<sub>4</sub>. In this study, we modified g-C<sub>3</sub>N<sub>4</sub> using multi-site Sr-doping from the surface to the interlayer and then to the bulk phase of g-C<sub>3</sub>N<sub>4</sub>. We found that this multi-site Sr-doping improves the transfer efficiency of photogenerated carriers and enables the activation of H<sub>2</sub>O<sub>2</sub> to produce more ·OH for complete NO removal. As a result, NO can be oxidized effectively and thoroughly. The verification and mechanism of this modification were explored in detail.

## 2. Experimental section

### 2.1. Preparation of photocatalysts

Both Melamine and strontium nitrate were purchased from Sinopharm Chemical Reagent Co., Ltd. All chemicals were of analytical grade and used without further purification.

To synthesize the multi-site Sr-doped carbon nitride, 4.0 g of melamine was firstly mixed with a certain amount of strontium nitrate (0.025 g, 0.05 g and 0.075 g). Then, the mixtures were ground uniformly in an agate mortar. Subsequently, the ground mixtures were transferred in a 30 ml crucible, which was then covered with a lid and placed in a muffle furnace for the calcination process. After the calcination at 520 °C for 4 h, the resulting sample was ground into powder and labeled as CNSrx ( $x = 0.025, 0.05, 0.075$ ). For comparison, pure carbon nitride (g-C<sub>3</sub>N<sub>4</sub>) was synthesized by calcining melamine under the same conditions but without the addition of strontium nitrate.

### 2.2. Evaluation of photocatalytic activity

The photocatalytic activities of the resulting samples were investigated using the NO removal experiments. The photocatalytic NO removal experiments were performed in a continuous reactor, and the schematic diagram of the NO removal experiment can be found in Fig. S1 (In the Supporting information). First, 50 mg of the catalyst was dispersed in 10 ml of deionized water and dispersed evenly in an ultrasonic bath for 15 min. Then, the catalyst suspension was poured into a glass dish ( $R = 3$  cm) and dried in an oven at 60 °C. This dish was placed in the middle of a cylindrical glass reactor ( $R = 5$  cm,  $H = 10$  cm,  $V = \pi \times R^2 \times H = 0.785$  L), which contained a gas inlet, a gas outlet and a quartz skylight. The air stream containing 600 ppb of NO continuously flowed over the surface of the sample. When the concentration of NO reaches a maximum value and maintains this value steadily, the adsorption-desorption equilibrium between the sample and NO is established. After the establishment of the adsorption-desorption equilibrium between the sample and NO, the sample was irradiated by visible light, which came through the quartz skylight and was generated from a 300 W Xe lamp with a 420 nm cut-off filter. During the entire process, the concentration of NO was monitored by the NOx analyzer (Thermo Model 42i).

### 2.3. The detection of active species

The H<sub>2</sub>O<sub>2</sub> was tested using the fluorescence method as follows. 0.1 g of sample powder was added in a 200 ml beaker that contained 100 ml of deionized water to form a sample suspension. Then, this suspension was irradiated by visible light under continuous stirring. In the irradiation process, the beaker was kept in an ice-water bath. During irradiation, 3 ml of the suspension was taken from the beaker every 10 min. This suspension was centrifuged and the sample partials were removed. Subsequently, 50 µl of fluorescent reagent (the preparation of which is in the supporting information) was added to react with the generated H<sub>2</sub>O<sub>2</sub>. After 10 min, 1 ml of a NaOH solution was added to end the reaction. Finally, the H<sub>2</sub>O<sub>2</sub> concentration was measured by a fluorescence spectrophotometer (emitted at 409 nm and excited at 315 nm).

As for the test of the ·OH, 0.05 g of the sample was dispersed into 50 ml of terephthalic acid solution (1.25 Mmol/l) under stirring. Then, after turning on the visible light, 4 ml of the suspension was taken from the reacting beaker every 10 min. This suspension was centrifuged and the sampled partials were removed for the fluorescence test (emitted at 426 nm and excited at 312 nm).

### 2.4. DFT calculation

To better understand the effects of the introduced Sr for the structure and activity of g-C<sub>3</sub>N<sub>4</sub>, the first principle calculation was used to calculate the systematic energy, the band structure, the O<sub>2</sub> activation, and the H<sub>2</sub>O<sub>2</sub> activation of different samples. The first principle calculation was performed using density functional theory (DFT) in the Cambridge sequential total energy package (CASTEP) module and calculated within the generalized gradient approximation of the Perdew-Burke-Ernzerhof (GGA-PBE) [21,22]. In the calculation process, the cut off energy was set to 240 eV, and the geometric optimization and properties were calculated using a  $1 \times 1 \times 1$  Monkhorst-Pack K point [23]. The Heyd-Scuseria-Ernzerhof (HSE06) hybridization function was used to obtain the exact band structure.

## 3. Results and discussion

The photocatalytic activity of the g-C<sub>3</sub>N<sub>4</sub> and CNSrx samples were investigated by the NO removal experiments. As shown in Fig. 1a, the NO removal efficiency increases from 37% to 55% with the increase of the Sr doping amount from 0 to 0.05 g. The removal rate constant of CNSr0.05 ( $0.24 \text{ min}^{-1}$ ) is 1.5 times higher than that of g-C<sub>3</sub>N<sub>4</sub> ( $0.16 \text{ min}^{-1}$ ). However, the continued increase of the Sr doping amount can decrease the NO removal efficiency. These results indicate that the doping of a moderate amount of Sr is helpful to enhancing the photocatalytic NO removal activity of g-C<sub>3</sub>N<sub>4</sub>.

In addition to NO removal, we also detected the generated NO<sub>2</sub> in the g-C<sub>3</sub>N<sub>4</sub> and CNSr0.05 systems. As shown in Fig. 1b, the NO<sub>2</sub> yield in the g-C<sub>3</sub>N<sub>4</sub> and CNSr0.05 systems are 155.8 and 76.2 ppb, respectively. According to Fig. 1c, the removed quantities of NO in the g-C<sub>3</sub>N<sub>4</sub> and CNSr0.05 systems are 253 and 481 ppb, respectively. Therefore, the NO<sub>2</sub> conversion rates (Fig. 1d) in the g-C<sub>3</sub>N<sub>4</sub> and CNSr0.05 systems are calculated to be 62.5% and 15.8%, respectively. This result shows that the main product of the NO removal in the g-C<sub>3</sub>N<sub>4</sub> and CNSr0.05 systems is NO<sub>2</sub> and NO<sub>3</sub><sup>-</sup>, respectively. The main product of NO<sub>3</sub><sup>-</sup> in the CNSr0.05 system can be verified by ion chromatography (Fig. S2, in Supporting information). Moreover, the generated NO<sub>2</sub> and NO<sub>3</sub><sup>-</sup> could meet the consummation of NO (This calculation of N-balance can be found in supporting information). And after five cycles of testing (Fig. S3b, in Supporting information), although the activity of CNSr0.05 was slightly reduced, it was still much more active than the original g-C<sub>3</sub>N<sub>4</sub>.

It is well known that the performance of a photocatalyst depends on its structure. Therefore, we first studied the influence of the Sr on the structure of g-C<sub>3</sub>N<sub>4</sub> using X-ray diffraction (XRD), a scanning electron

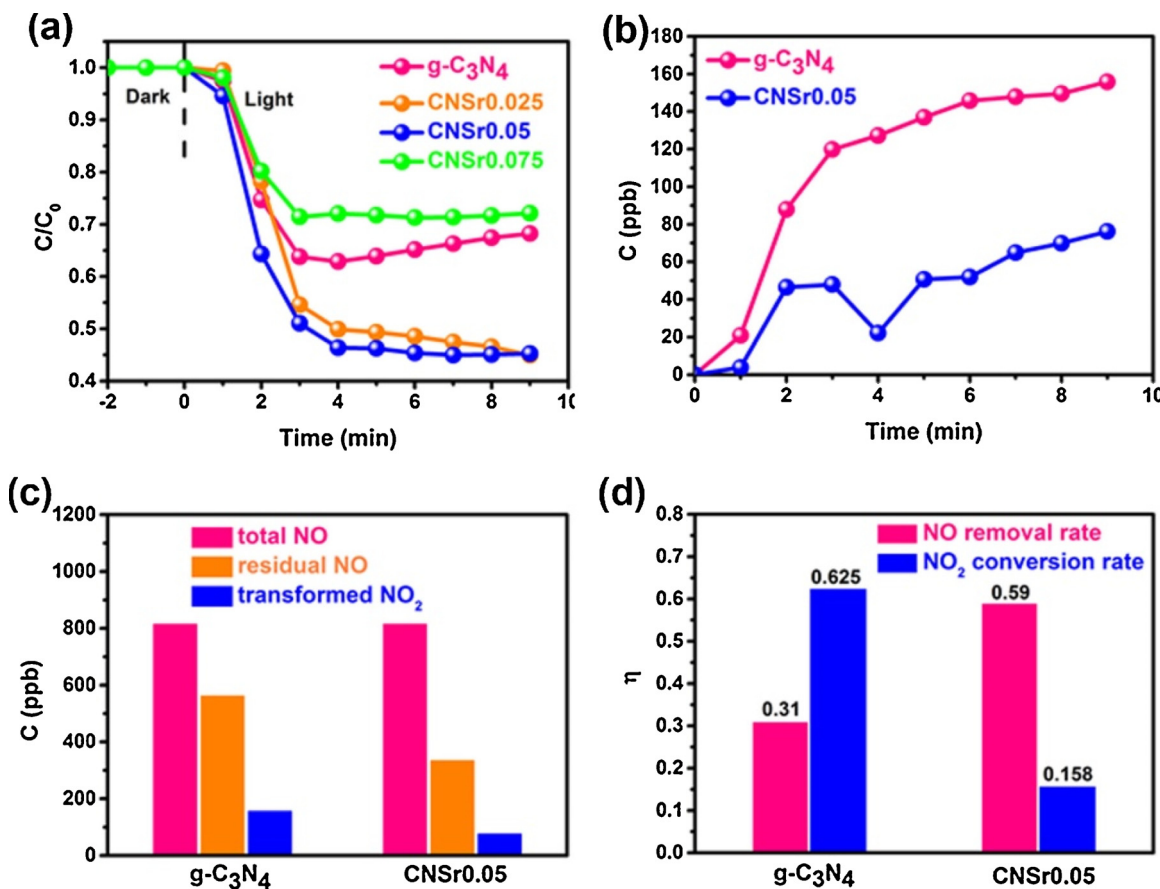


**Fig. 1.** The NO removal of CNSrx samples (a); NO<sub>2</sub> generation in  $\text{g-C}_3\text{N}_4$  and CNSr0.05 systems (b); the amount changes of NO and NO<sub>2</sub> in  $\text{g-C}_3\text{N}_4$  and CNSr0.05 systems (c); removal of NO and conversion rate of NO<sub>2</sub> in  $\text{g-C}_3\text{N}_4$  and CNSr0.05 systems (d).

microscope (SEM), X-ray photoelectron spectrometry (XPS), and the DFT calculation.

The XRD measurements were used to investigate the phase structure of the resulting samples. As shown in Fig. 2a, the XRD curve of pure  $\text{g-C}_3\text{N}_4$  is well matched with JCPDS No 87-1522. Two characteristic peaks contained in this curve at  $13.1^\circ$  and  $27.4^\circ$  correspond to the (100) and (002) crystal planes of  $\text{g-C}_3\text{N}_4$ , respectively [24]. The small peak at  $13.1^\circ$  corresponds to the in-plane array of tri-s-triazine units, while the peak at  $27.4^\circ$  is due to the inter-planar stacking in the vertical direction [25,26]. As for the CNSrx samples, no other impurity peaks besides above two peaks appear in their XRD curves. Compared with the XRD curve of  $\text{g-C}_3\text{N}_4$ , the peak at  $27.4^\circ$  of the CNSr samples shifted toward a bigger degree with the increase of  $\text{Sr}(\text{NO}_3)_2$  (Fig. 2b), indicating that Sr doping could decrease the layer distance of  $\text{g-C}_3\text{N}_4$ . Meanwhile, this phenomenon also implies that some of the Sr atoms have intercalated in the interlayer of  $\text{g-C}_3\text{N}_4$ . This suspension is based on two reasons (Fig. 2c): (1) the interlaminar Sr may weaken the repulsive force between two adjacent layers, and (2) the interlaminar Sr may attract the negatively charged N in the (002) crystal plane.

According to the geometric construction of  $\text{g-C}_3\text{N}_4$ , the interlayer spacing of  $\text{g-C}_3\text{N}_4$  is  $3.16 \text{ \AA}$  (Fig. 2d) [27,28], which is much bigger than the diameter of the Sr ion ( $2.24 \text{ \AA}$ ). Meanwhile, the cavity size of  $\text{g-C}_3\text{N}_4$  ( $4.74 \text{ \AA}$ ) is also bigger than the diameter of the Sr atom (Fig. 2e). And since the 4d orbital of Sr is an empty orbit, both C and N have lone pairs of electrons, then Sr can accept the lone pair of C or N to form a coordination bond with it, so Sr may be in the form of replacing C or N (Fig. S4, in Supporting information). Therefore, the doping method of Sr has many possibilities. Sr may intercalate in the interlayer of  $\text{g-C}_3\text{N}_4$ , fill in the cavity of  $\text{g-C}_3\text{N}_4$ , or replace some  $\text{g-C}_3\text{N}_4$  atoms. To investigate the doping method of Sr in the CNSrx structure, DFT calculations were

used to investigate the required energy for several possible doping positions based on the following equation:

$$E = E_{ca} - E_{CN} - E_{Sr}$$

where  $E_{ca}$  is the energy of the possible structure calculated by DFT,  $E_{CN}$  is the energy of  $\text{g-C}_3\text{N}_4$  ( $-12363.6773 \text{ eV}$ ), and  $E_{Sr}$  is the energy of Sr ( $-835.1120 \text{ eV}$ ). The calculation results were summarized in Fig. 3. From this figure, the substitution of C with Sr needs approximately  $765 \text{ eV}$  of energy, thus implying that the replacement of C with Sr is hard to realize. In addition to C replacement, four other doping methods including interlayer intercalation, cavity padding, the replacement of the bridging N and the replacement of triazine N are energy-releasing process, thus indicating that these four doping methods are possible. Since the replacement of the bridging N can release the most energy, we speculate that the replacement of the bridging N is the main doping method of Sr. However, because the other three doping methods including interlayer intercalation, cavity padding, and the replacement of triazine N are energy releasing processes, there are still a few Sr atoms existing in the interlayer, the cavity or the position of triazine N. Hence, the doping of Sr is a multi-site doping from the surface to the interlayer and then to the bulk phase of  $\text{g-C}_3\text{N}_4$ . The presence of Sr in different locations can be verified by other experiments in the latter parts.

The morphologies and microstructures of  $\text{g-C}_3\text{N}_4$  and CNSr0.05 were observed by SEM. As shown in Fig. 4a, the pure  $\text{g-C}_3\text{N}_4$  shows a distinct layered structure, which is consistent with previous reports [29]. After the incorporation of Sr, the overall structure of CNSr0.05 is similar to that of the pure  $\text{g-C}_3\text{N}_4$  (Fig. 4b), suggesting that the incorporation of Sr does not significantly affect the morphology of  $\text{g-C}_3\text{N}_4$ . However, the layered structure seems to become denser after the

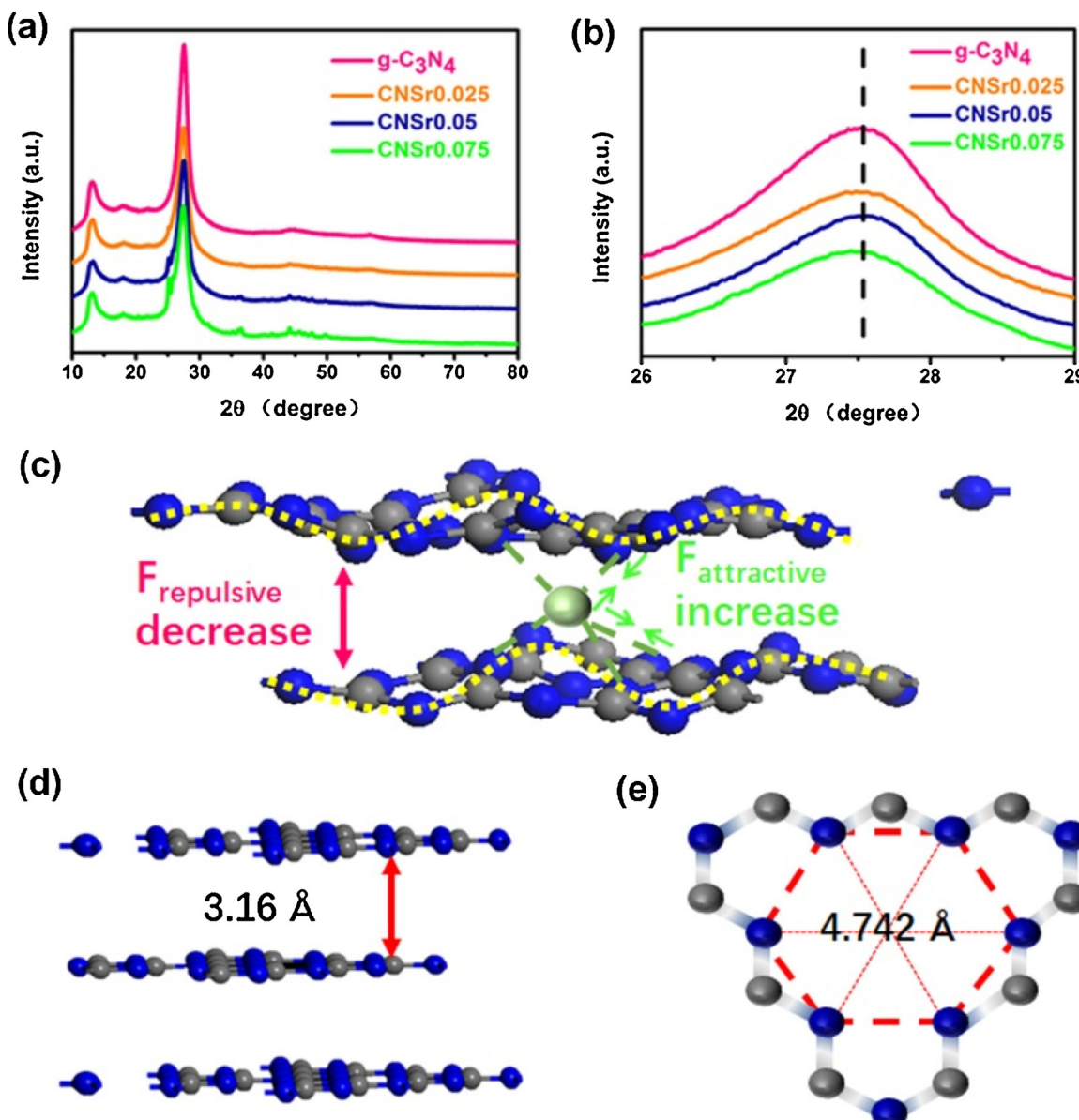


**Fig. 2.** XRD spectra of different samples (a) and enlargement XRD spectra (b); the reduced layer spacing (c); layer spacing of  $\text{g-C}_3\text{N}_4$  (d); cavity size of  $\text{g-C}_3\text{N}_4$  (e).

incorporation of the Sr ion, which is consistent with the XRD result that the layer distance of the CNSrx has decreased. To examine the distribution of Sr on the surface of the CNSr sample, SEM-EDS (Fig. 4c and d) was used to investigate the elemental mapping images of the Sr. It is observed that the Sr element is uniformly distributed on the surface of the CNSr0.05 structure. The existence of Sr on the surface of the CNSr0.05 can also be confirmed by the comparisons of XPS patterns (Fig. S5, the detail analysis of XPS can be found in supporting information). The surface distribution of the Sr can be explained by three doping methods, including the replacement of the bridging N, the replacement of the triazine N, and cavity padding. To examine if the Sr element can exist in the interlayer of the CNSr sample, the high-resolution Sr 3d XPS depth profile analysis was employed to monitor the amount of the changes of the Sr in the inner region of the CNSr0.05. From Fig. 4e, the intensity of the Sr 3d XPS in the inner regions is higher than that on the surface region. This phenomenon indicates that the Sr elements can not only distribute in the in-planar of  $\text{g-C}_3\text{N}_4$  but can also exist in the interlayer of  $\text{g-C}_3\text{N}_4$ .

The large specific surface area and abundant pore structure can provide more active sites for the photocatalytic reaction, thereby

improving the removal efficiency of NO [30]. Therefore, to discover the reason for the improved NO removal activity, specific surface areas of the result samples were firstly tested by measuring the amount of adsorbed  $\text{N}_2$  in the different samples. Fig. 5a shows the  $\text{N}_2$  adsorption-desorption isotherms of different samples. The isotherms of both samples are type III adsorption-desorption isotherms. Moreover, both isotherms display type H3 hysteresis loops, suggesting that the pores of both samples are actually the slits between plate-like particles [31]. The BET surface areas of  $\text{g-C}_3\text{N}_4$  and CNSr0.05 are calculated to be 6.3 and  $7.5 \text{ m}^2/\text{g}$ , respectively. Based on the adsorption-desorption isotherms and BET surface areas, we can conclude that the doping of Sr does not significantly affect the surface area of  $\text{g-C}_3\text{N}_4$ . Therefore, the fact that Sr multi-site doping enhanced the photocatalytic NO removal activity of  $\text{g-C}_3\text{N}_4$  is not related to the surface area.

In addition to the surface area, the optical property can affect the photocatalytic activity of the photocatalyst because the electron excitation in the photocatalysis is dependent on the light absorption. Therefore, an Ultraviolet-visible (UV-vis) spectrophotometer was used to analyze the optical properties of the two samples. Fig. 5b shows the UV-vis absorption spectra of two samples. Compared with  $\text{g-C}_3\text{N}_4$ , the

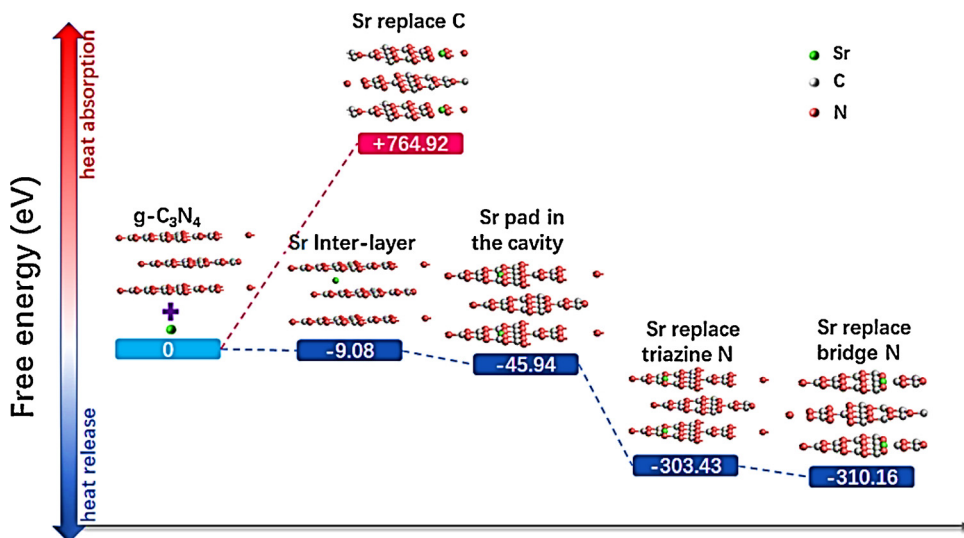


Fig. 3. The heat absorption and release of various possible structures in DFT calculation.

UV-vis absorption spectrum of CNSr0.05 has a red shift of approximately 11 nm, indicating that the doping of Sr can broaden the light absorption region of g-C<sub>3</sub>N<sub>4</sub>. Not only that, the doping of Sr can also decrease the band gap of g-C<sub>3</sub>N<sub>4</sub> from 2.79 eV to 2.77 eV (Fig. 5c). This result is consistent with the results of DFT calculation that all the doping modals of Sr could decrease the band gap of g-C<sub>3</sub>N<sub>4</sub> (Fig. 5d-h). Doping modals including intercalation, cavity padding, and replacement of triazine N can lead to the generation of impurities in the band gap of g-C<sub>3</sub>N<sub>4</sub> (Fig. 5d-g). These impurities extend the valence band or conduction band into the bandgap, and narrow the bandgap. Therefore, in the same condition, the CNSrx can produce more electron and hole pairs.

After the generation of electron and hole pairs, electrons and holes should separate and migrate to the surface of the photocatalyst. The higher separation efficiency and migration rate would result in better photocatalytic performance. The photoluminescence (PL) is very useful to investigate the separation efficiency of the electron and hole pairs. According to the mechanism of the emissions spectrum, a lower emissions peak corresponds to a higher separation efficiency [32–34]. From Fig. 6a, the PL intensity of CNSr0.05 is obviously lower than that of g-C<sub>3</sub>N<sub>4</sub>, suggesting that the intercalation of Sr can improve the separation efficiency of electron and hole pairs. To further investigate the migration efficiency of the photogenerated carriers in different samples, electrochemical impedance spectroscopy (EIS) was performed using a

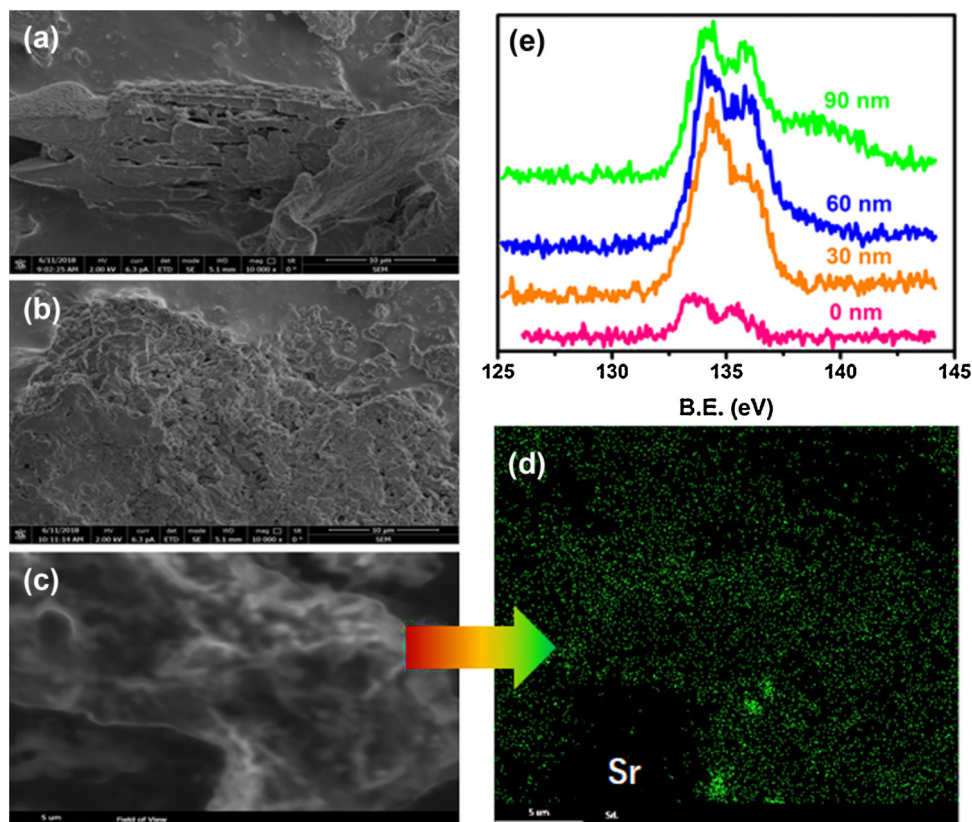
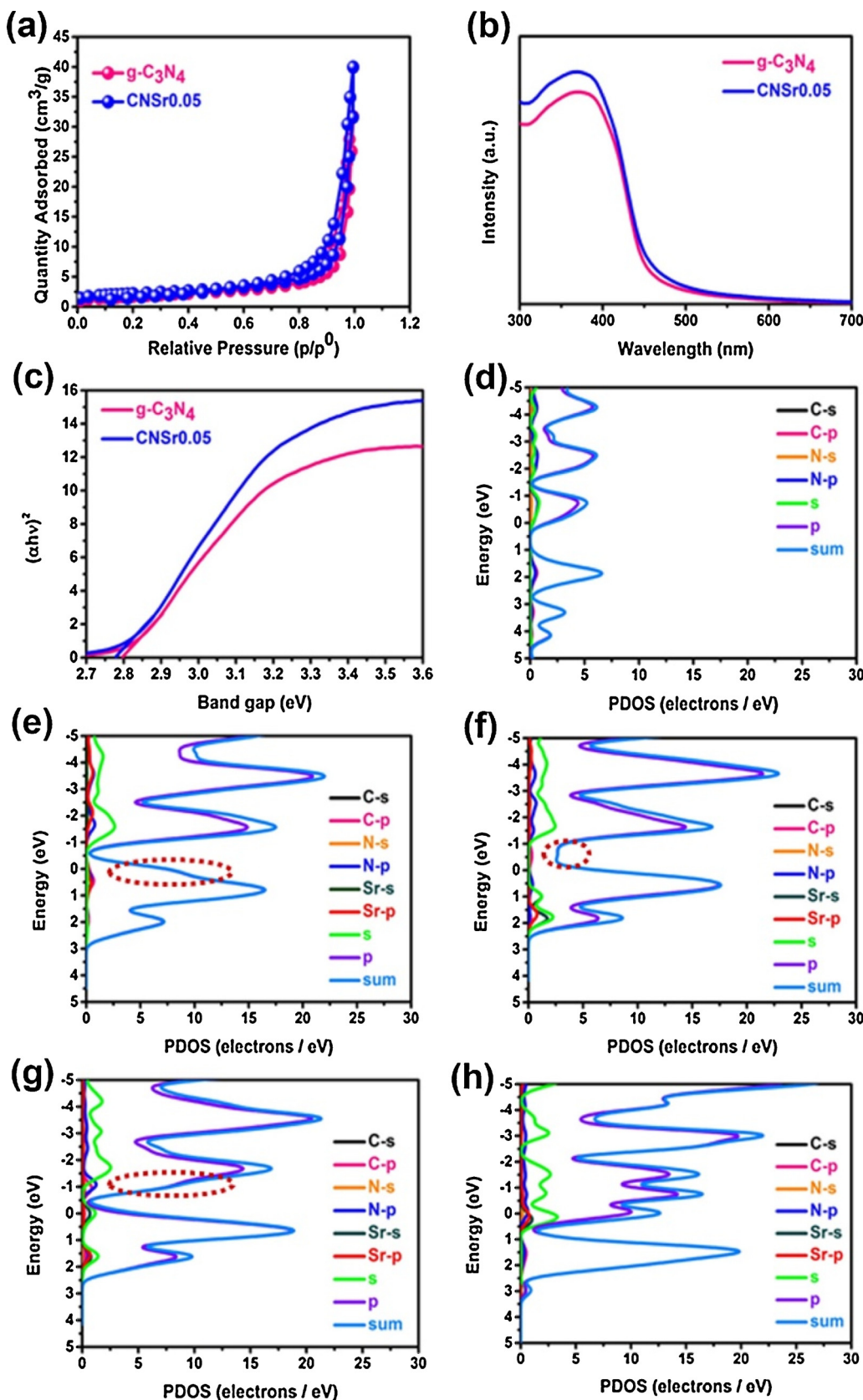
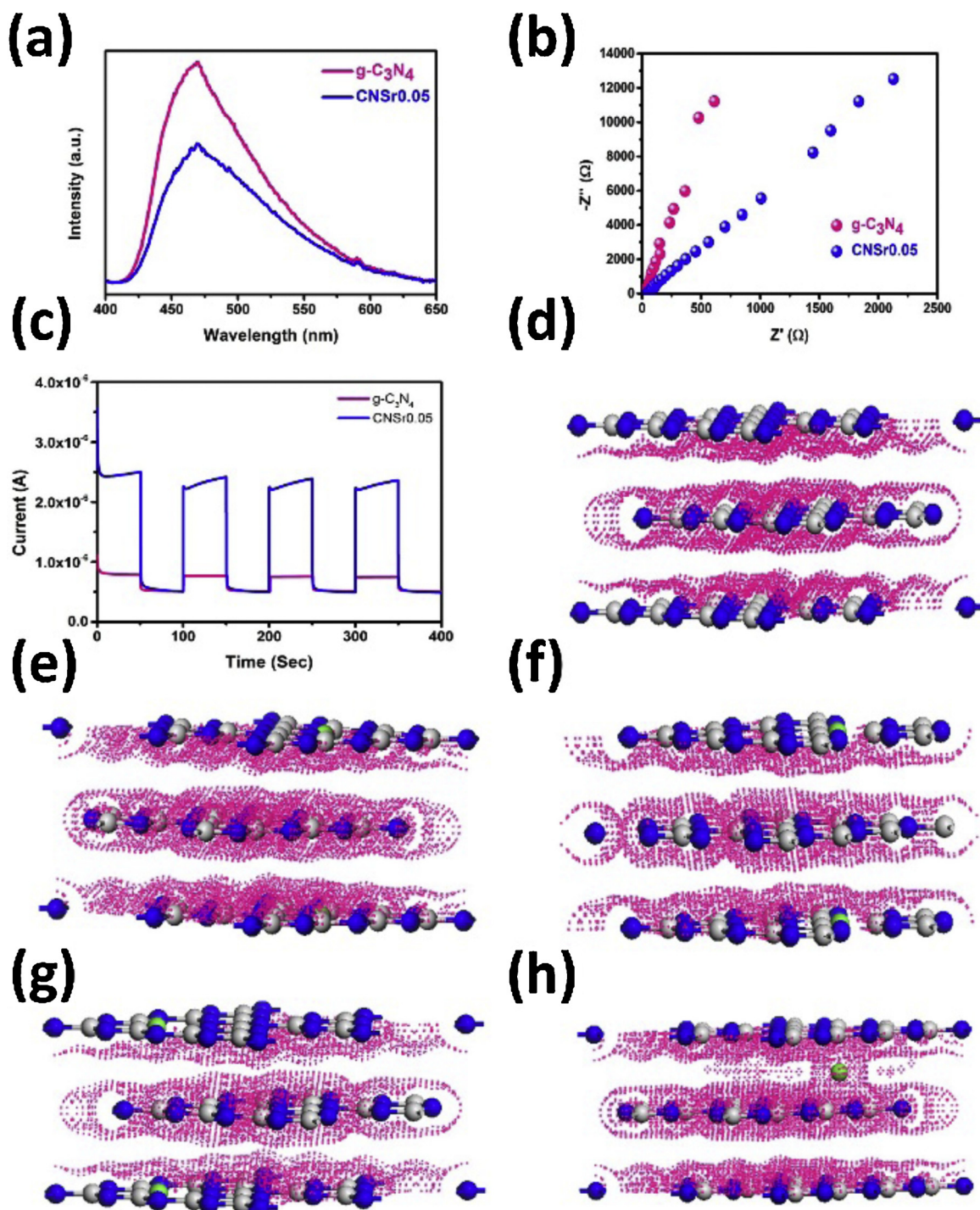


Fig. 4. The SEM images of g-C<sub>3</sub>N<sub>4</sub> (a) and CNSr0.05 (b, c); and SEM-EDS element mapping of CNSr0.05 (d); Sr 3d XPS depth analysis of CNSr0.05 (e).



**Fig. 5.** N<sub>2</sub> adsorption-desorption isotherms (a); UV-vis absorption spectra (b); UV-vis diffuser reflectance spectra of g-C<sub>3</sub>N<sub>4</sub> and CNSr.05(c); partial density of states (PDOS) of g-C<sub>3</sub>N<sub>4</sub> (d); Sr intercalated g-C<sub>3</sub>N<sub>4</sub> (e); Sr cavity padded g-C<sub>3</sub>N<sub>4</sub> (f); triazine N was replaced g-C<sub>3</sub>N<sub>4</sub> (g); bridge N was replaced g-C<sub>3</sub>N<sub>4</sub> (h).



**Fig. 6.** The PL spectra (a), EIS spectra (b) photocurrent data (c) of g-C<sub>3</sub>N<sub>4</sub> and CNSr0.05; electron density distribution of g-C<sub>3</sub>N<sub>4</sub> (d); Sr cavity padded g-C<sub>3</sub>N<sub>4</sub> (e); bridge N was replaced g-C<sub>3</sub>N<sub>4</sub> (f); triazine N was replaced g-C<sub>3</sub>N<sub>4</sub> (g); Sr intercalated g-C<sub>3</sub>N<sub>4</sub> (h).

three-electrode system. The smaller the arc radius of the EIS Nyquist plot, the better the migration efficiency of the photogenerated carriers [35–38]. From Fig. 6b, the circular arc radius on the EIS Nyquist plot of CNSr0.05 is significantly smaller than that of pure CN, indicating that the migration efficiency of carriers is obviously improved by the Sr intercalation. This conclusion can also be confirmed by the photocurrent result as shown in Fig. 6c. And the reason can be revealed by the DFT calculation. After the calculation, we found that the replacement of N atoms and cavity padding have no effect on the electron transport of the sample (Fig. 6e–g). However, it is surprising that the

intercalation of Sr can form an interlayer electron channel that links two adjacent layers formed around the intercalary Sr atom (Fig. 6h). This channel makes the electron migration from one layer to another layer become easier, which is why the Sr doping can improve the carrier migration of g-C<sub>3</sub>N<sub>4</sub>.

In addition to the numbers of surface holes and electrons, the photocatalytic activity of one photocatalyst is also impacted by the redox potential of the surface holes and electrons. Therefore, the valence band XPS spectra were measured to analyze the valence band potentials of different samples. As shown in Fig. 7a, the valence band

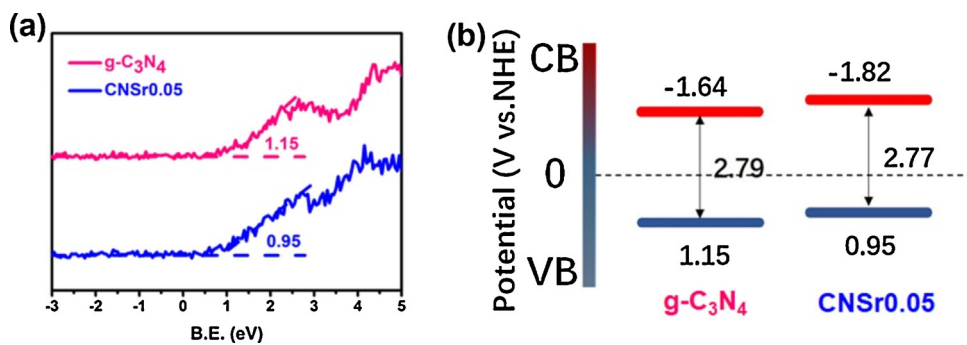


Fig. 7. XPS valence spectra (a), band gap diagram of  $\text{g-C}_3\text{N}_4$  and CNSr0.05 samples (b).

Table 1

Bond length after  $\text{O}_2$  activation in various possible structures (the original bond length of  $\text{O}_2$  is 1.21 Å).

Structure	$\text{g-C}_3\text{N}_4$	Replace triazine N	Replace bridge N	Inter-layer	Pad in the cavity
Bond length (Å)	1.263	3.671	3.308	1.286	1.305

potentials ( $E_V$ ) of  $\text{g-C}_3\text{N}_4$  and CNSr0.05 are 1.13 and 0.99 eV, respectively. Then, the conduction band potential ( $E_C$ ) can be calculated through the formula  $E_g = E_V - E_C$  [39]. The calculated results show that the CB of  $\text{g-C}_3\text{N}_4$  and CNSr0.05 are  $-1.66$  and  $-1.78$  eV, respectively. Therefore, the doping of Sr could increase both the valence band and conduction band (Fig. 7b). This conclusion can also be confirmed by the DFT calculation (Fig. 5d-h). According to the DFT calculation results, except for the doping manner of the bridge N substitution, other possible doping manners could generate impurities and increase the VB and CB, leading to an increase of the reduction ability of the photo-generated electrons, thus producing more reactive oxygen species

through the following pathways:



The generation of  $\cdot\text{O}_2^-$  in the samples before and after the modification was tested using electron paramagnetic resonance (EPR) as shown in Fig. S6 (In Supporting information). Both  $\text{g-C}_3\text{N}_4$  and CNSr0.05 exhibit the characteristic peaks of  $\cdot\text{O}_2^-$ . Moreover, the peak intensity of the CNSr0.05 is much higher than that of  $\text{g-C}_3\text{N}_4$ , indicating the doping of the Sr sample has a great effect on the activation of oxygen. We further used DFT calculations to simulate the activation of oxygen in different sample structures. From Table 1 and Fig. 8a-e,  $\text{O}_2$  cannot be activated on the surface of  $\text{g-C}_3\text{N}_4$  because the O–O bond length has almost no change before and after structural optimization. Meanwhile, the Sr doping manners of intercalation and cavity padding have a tiny effect on the activation of  $\text{O}_2$ . However, the doping manner of the replacement of the triazine N and the bridging N was found to help the activation of  $\text{O}_2$ . The O–O bond length was significantly increased from 1.24 Å to 3.671 Å and 3.308 Å, respectively. It is possible that the Sr

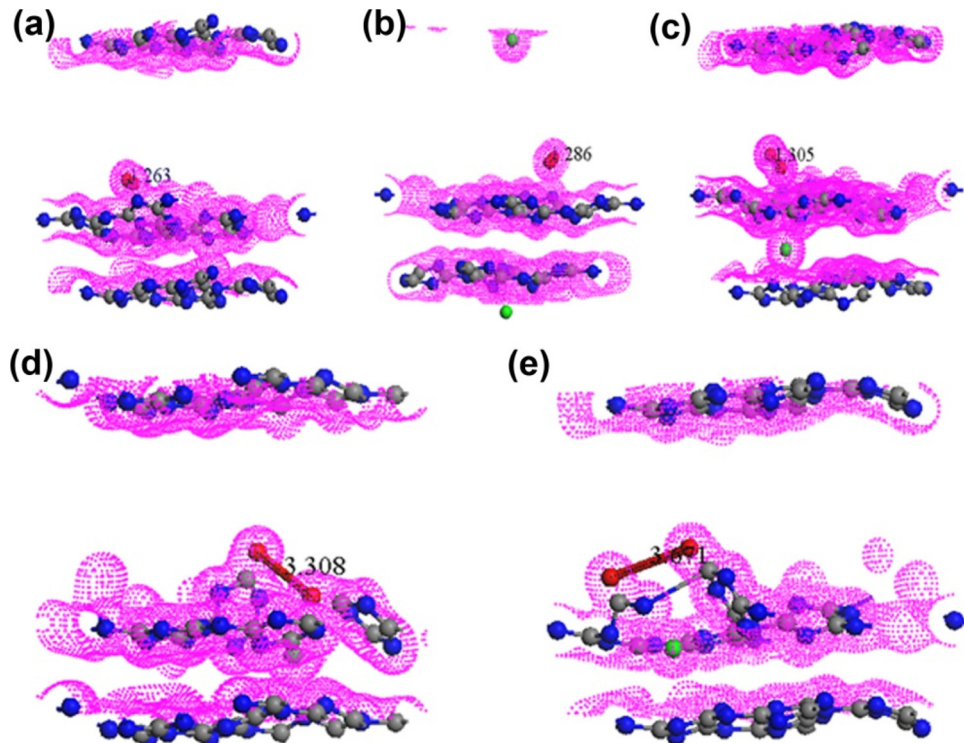


Fig. 8. Activation of  $\text{O}_2$  in various possible structure in DFT calculation:  $\text{g-C}_3\text{N}_4$  (a); Sr intercalated  $\text{g-C}_3\text{N}_4$  (b); Sr cavity padded  $\text{g-C}_3\text{N}_4$  (c); bridge N was replaced  $\text{g-C}_3\text{N}_4$  (d); triazine N was replaced  $\text{g-C}_3\text{N}_4$  (e).

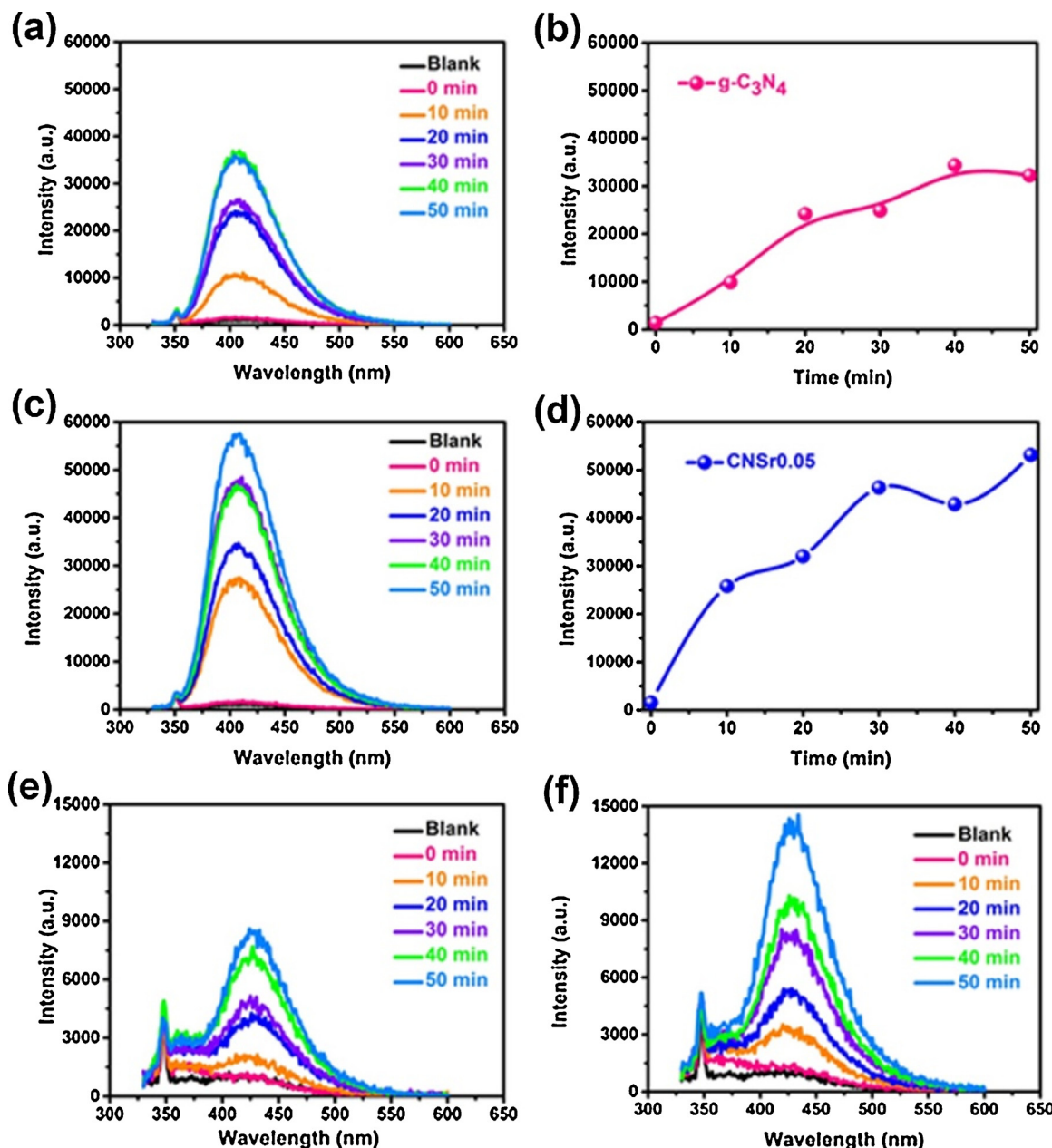
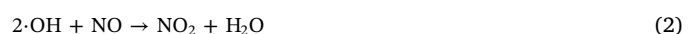


Fig. 9. H<sub>2</sub>O<sub>2</sub> production of g-C<sub>3</sub>N<sub>4</sub> (a–b) and CNSr0.05 (c–d); ·OH production of g-C<sub>3</sub>N<sub>4</sub> (e) and CNSr0.05 (f).

doped on the surface enhances the adsorption ability of the catalyst surface to O<sub>2</sub>, and the electron transport channels formed by the Sr between the layers can make electrons more easily reach the surface, thereby reducing more O<sub>2</sub> to ·O<sub>2</sub><sup>-</sup>.

From Fig. 9a and b, the signal intensity of the generated H<sub>2</sub>O<sub>2</sub> in g-C<sub>3</sub>N<sub>4</sub> is generally increased, indicating that the decomposition of H<sub>2</sub>O<sub>2</sub> in the g-C<sub>3</sub>N<sub>4</sub> system does not happen or is very small. In the CNSr0.05 system (Fig. 9c and d), the signal intensity of the generated H<sub>2</sub>O<sub>2</sub> begins to fluctuate at 40 min, suggesting that the decomposition of H<sub>2</sub>O<sub>2</sub> in the CNSr0.05 system is very significant. According to previous reports, the decomposition of H<sub>2</sub>O<sub>2</sub> may produce ·OH [40,41]. For the complete oxidation of NO, hydroxyl radicals play an important role. Therefore, we speculate that the CNSr0.05 system may produce a large amount of ·OH, while the g-C<sub>3</sub>N<sub>4</sub> system may produce very little ·OH. To test this hypothesis, we measured and compared the generated ·OH in two sample systems. As shown in Fig. 9e and f, the ·OH generated in the CNSr0.05 system is significantly more than that in the g-C<sub>3</sub>N<sub>4</sub> system. This difference can be explained by the DFT calculations. We used the

DFT calculations to simulate the activation of H<sub>2</sub>O<sub>2</sub> in different possible structures. The results are shown in Fig. 10 and Table 2 below. From Fig. 10a, H<sub>2</sub>O<sub>2</sub> cannot be activated on the surface of g-C<sub>3</sub>N<sub>4</sub> because the bond length of the H<sub>2</sub>O<sub>2</sub> has almost no change before and after structural optimization. Meanwhile, the Sr doping manners of the intercalation and the N atom replacement do not help the activation of the H<sub>2</sub>O<sub>2</sub> on the surface of the CNSr (Fig. 10b–d). However, the doping manner of the cavity padding was found to help the activation of the H<sub>2</sub>O<sub>2</sub> (Fig. 10e). After the structural optimization, the O–O bond length of the H<sub>2</sub>O<sub>2</sub> was expanded from 1.480 to 4.050 Å. This calculation result explained why the CNSr0.05 system could produce much more ·OH than g-C<sub>3</sub>N<sub>4</sub>. Furthermore, it also confirms the presence of Sr doping manners with the cavity padding. And based on the above research, propose a possible NO removal reaction mechanism, as shown in the following equation:



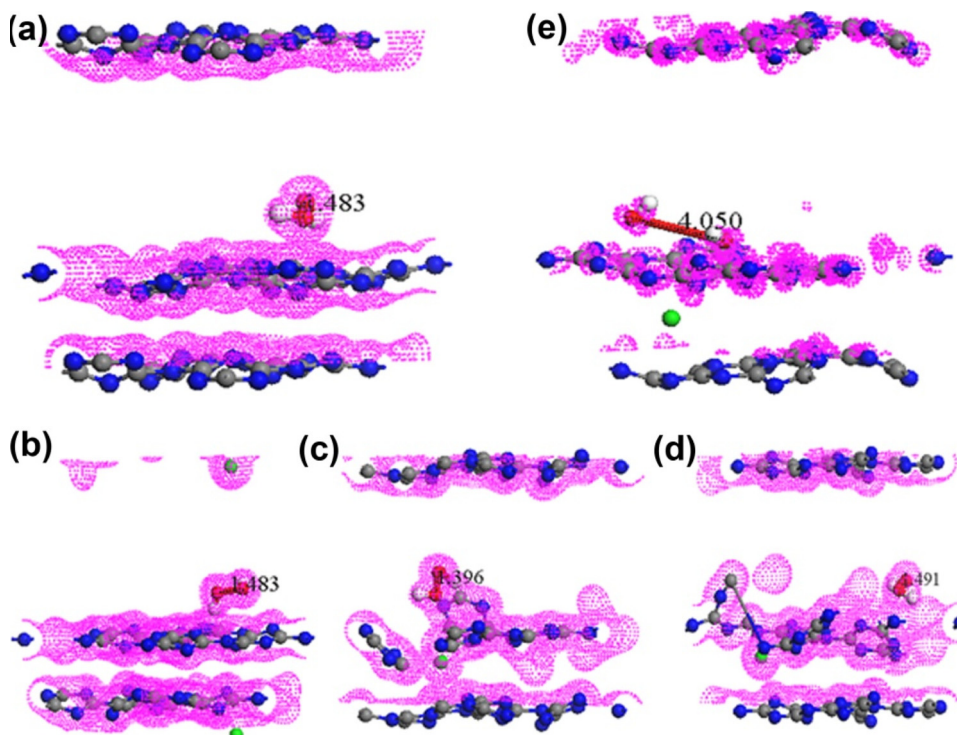


**Fig. 10.** Activation of  $\text{H}_2\text{O}_2$  in various possible structure in DFT calculation: g-C<sub>3</sub>N<sub>4</sub> (a); Sr intercalated g-C<sub>3</sub>N<sub>4</sub> (b); bridge N was replaced g-C<sub>3</sub>N<sub>4</sub> (c); triazine N was replaced g-C<sub>3</sub>N<sub>4</sub> (d); Sr cavity padded g-C<sub>3</sub>N<sub>4</sub> (e).

**Table 2**

Bond length after  $\text{H}_2\text{O}_2$  activation in various possible structures (the original O–O bond length of  $\text{H}_2\text{O}_2$  is 1.480 Å).

Structure	g-C <sub>3</sub> N <sub>4</sub>	Replace triazine N	Replace bridge N	Inter-layer	Pad in the cavity
Bond length (Å)	1.483	1.396	1.396	1.483	4.050



#### 4. Conclusion

We designed the multi-site doping of Sr for the efficient and complete NO removal using a g-C<sub>3</sub>N<sub>4</sub> based photocatalyst. Through a one-step thermal polymerization reaction, the multi-site Sr-doped g-C<sub>3</sub>N<sub>4</sub> was successfully synthesized to remove the low concentrated NO under visible light irradiation. The results show that the multi-site doping of Sr could improve the NO removal rate by 1.5 times. Meanwhile, the conversion rate of secondary pollution ( $\text{NO}_2$ ) was decreased from 62.5% to 15.8% by the multi-site doping of Sr. In the multi-site doping of Sr, the effects of the doped Sr are different with different doping modes. All the doping modal of Sr including intercalation, cavity padding, replacement of triazine N and bridging N could decrease the band gap of g-C<sub>3</sub>N<sub>4</sub>. Meanwhile, the Sr that intercalated in the interlayer of g-C<sub>3</sub>N<sub>4</sub> could improve the transfer of photogenerated electrons by forming a charge channel between two crystal planes, the Sr that replaced the N atoms could help the activation of  $\text{O}_2$  to produce more  $\cdot\text{O}_2^-$ , and the Sr padded in the cavity provides g-C<sub>3</sub>N<sub>4</sub> with the ability to activate the  $\text{H}_2\text{O}_2$  for the generation of a stronger oxidant ( $\cdot\text{OH}$ ), which could deeply oxidize NO to  $\text{NO}_3^-$ . Different doping modes complement each other, and combine to realize the efficient and complete removal of NO together.

#### Acknowledgment

Financial support by the National Nature Science Foundation of China (Grant No. 21876104 and 21603271) are gratefully appreciated.

#### Appendix A. Supplementary data

Supplementary material related to this article can be found, in the online version, at doi:<https://doi.org/10.1016/j.apcatb.2019.117825>.

#### References

- [1] G. Pascal, I.P. Vasile, Catalytic NOx abatement systems for mobile sources: from three-way to lean burn after-treatment technologies, *Chem. Rev.* 111 (2011) 3155–3207.
- [2] G.H. Dong, L.J. Daniel, L. Zang, C.Y. Wang, Carbon vacancy regulated photo-reduction of NO to  $\text{N}_2$  over ultrathin g-C<sub>3</sub>N<sub>4</sub> nanosheets, *Appl. Catal. B: Environ.* 218 (2017) 515–524.
- [3] Y. Liu, J. Zhao, J.M. Lee, Conventional and new materials for selective catalytic reduction (SCR) of NOx, *ChemCatChem* 10 (2017) 1499–1511.
- [4] W. Zhou, W. David, L. Vitali, J.Y. Chen, Development and implementation of numerical simulation for a selective noncatalytic reduction system design, *Ind. Eng. Chem. Res.* 48 (2009) 10994–11001.
- [5] Z.Y. Wang, M.J. Chen, Y. Huang, X.J. Shi, Y.F. Zhang, T.T. Huang, J.J. Cao, W.K. Ho, S.C. Lee, Self-assembly synthesis of boron-doped graphitic carbon nitride hollow tubes for enhanced photocatalytic NOx removal under visible light, *Appl. Catal. B: Environ.* 239 (2018) 352–361.
- [6] J.Z. Ma, C.X. Wang, H. He, Enhanced photocatalytic oxidation of NO over g-C<sub>3</sub>N<sub>4</sub>-TiO<sub>2</sub> under UV and visible light, *Appl. Catal. B: Environ.* 184 (2016) 28–34.
- [7] Z.Y. Wang, Y. Huang, W.K. Ho, J.J. Cao, Z.X. Shen, S.C. Lee, Fabrication of Bi<sub>2</sub>O<sub>3</sub>CO<sub>3</sub>/g-C<sub>3</sub>N<sub>4</sub> heterojunctions for efficiently photocatalytic NO in air removal: in-situ self-sacrificial synthesis, characterizations and mechanistic study, *Appl. Catal. B: Environ.* 199 (2016) 123–133.
- [8] D. Liu, J. Wang, X.J. Bai, R.L. Zong, Y.F. Zhu, Self-assembled PDINH supramolecular system for photocatalysis under visible light, *Adv. Mater.* 28 (2016) 7284–7290.
- [9] Y.S. Jun, E.Z. Lee, X.C. Wang, W.H. Hong, D.S. Galen, T. Arne, From melamine-cyanuric acid supramolecular aggregates to carbon nitride hollow spheres, *Adv. Funct. Mater.* 23 (2013) 3661–3667.
- [10] S.W. Cao, J.X. Low, J.G. Yu, M. Jaroniec, Polymeric photocatalysts based on graphitic carbon nitride, *Adv. Mater.* 27 (2015) 1–27.
- [11] Y.M. Yu, J.F. Geng, H. Li, R.Y. Bao, H.Y. Chen, W.Z. Wang, J.X. Xia, W.Y. Wong, Exceedingly high photocatalytic activity of g-C<sub>3</sub>N<sub>4</sub>/Gd-N-TiO<sub>2</sub> composite with nanoscale heterojunctions, *Solar Energy Mater. Solar Cells* 168 (2017) 91–99.

- [12] M.Q. Wen, T. Xiong, Z.G. Zang, W. Wei, X.T. Tang, F. Dong, Synthesis of MoS<sub>2</sub>/g-C<sub>3</sub>N<sub>4</sub> nanocomposites with enhanced visible-light photocatalytic activity for the removal of nitric oxide (NO), Opt. Express 24 (2016) 10205–10212.
- [13] S.W. Liu, F. Chen, S.T. Li, X.X. Peng, Y. Xiong, Enhanced photocatalytic conversion of greenhouse gas CO<sub>2</sub> into solar fuels over g-C<sub>3</sub>N<sub>4</sub> nanotubes with decorated transparent ZIF-8 nanoclusters, Appl. Catal. B: Environ. 211 (2017) 1–10.
- [14] Y. Zheng, L.H. Lin, B. Wang, X.C. Wang, Graphitic carbon nitride polymers toward sustainable photoredox catalysis, Angew. Chem. Int. Ed. 54 (2015) 12868–12884.
- [15] M.Q. Chen, R.N. Guan, S.F. Yang, Hybrids of fullerenes and 2D nanomaterials, Adv. Sci. (2018) 1800941–1800967.
- [16] J.M. Luo, G.H. Dong, Y.Q. Zhu, Z. Yang, C.Y. Wang, Switching of semiconducting behavior from n-type to p-type induced high photocatalytic NO removal activity in g-C<sub>3</sub>N<sub>4</sub>, Appl. Catal. B: Environ. 214 (2017) 46–56.
- [17] Y.X. Li, S.X. Ouyang, H. Xu, X. Wang, Y.P. Bi, Y.F. Zhang, J.H. Ye, Constructing solid-gas-interfacial Fenton reaction over alkalinized-C<sub>3</sub>N<sub>4</sub> photocatalyst to achieve apparent quantum yield of 49% at 420 nm, J. Am. Chem. Soc. 138 (2016) 13289–13297.
- [18] L.B. Jiang, X.Z. Yuan, Y. Pan, J. Liang, G.M. Zeng, Z.B. Wu, H. Wang, Doping of graphitic carbon nitride for photocatalysis: a review, Appl. Catal. B: Environ. 2017 (2017) 388–406.
- [19] X.A. Dong, J.Y. Li, Q. Xing, Y. Zhou, H.W. Huang, F. Dong, The activation of reactants and intermediates promotes the selective photocatalytic NO conversion on electron-localized Sr-intercalated g-C<sub>3</sub>N<sub>4</sub>, Appl. Catal. B: Environ. 232 (2018) 69–76.
- [20] S. Jin, G.H. Dong, J.M. Luo, F.Y. Ma, C.Y. Wang, Improved photocatalytic NO removal activity of SrTiO<sub>3</sub> by using SrCO<sub>3</sub> as a new co-catalyst, Appl. Catal. B: Environ. 227 (2018) 24–34.
- [21] B.C. Zhu, L.Y. Zhang, B. Cheng, J.G. Yu, First-principle calculation study of tri-s-triazine-based g-C<sub>3</sub>N<sub>4</sub>: a review, Appl. Catal. B: Environ. 24 (2018) 983–999.
- [22] Y. Hou, M. Qiu, M.G. Kim, P. Liu, G. Nam, T. Zhang, X.D. Zhuang, J. Cho, M.W. Chen, C. Yuan, L.C. Lei, X.L. Feng, Atomically dispersed nickel–el–nitrogen–sulfur species anchored on porous carbon nanosheets for efficient water oxidation, Nat. Commun. 10 (2019) 1392.
- [23] H.J. Monkhorst, J.D. Pack, Special points for Brillouin-zone integrations, Phys. Rev. B 13 (1976) 5188–5192.
- [24] M. Karimi-Nazarabad, E.K. Goharshadi, Highly efficient photocatalytic and photoelectrocatalytic activity of solar light driven WO<sub>3</sub>/g-C<sub>3</sub>N<sub>4</sub> nanocomposite, Solar Energy Mater. Solar Cells 160 (2017) 484–493.
- [25] W.K. Ho, Z.Z. Zhang, M.K. Xu, X.W. Zhang, X.X. Wang, Y. Huang, Enhanced visible-light-driven photocatalytic removal of NO: effect on layer distortion on g-C<sub>3</sub>N<sub>4</sub> by H<sub>2</sub> heating, Appl. Catal. B: Environ. 179 (2015) 106–112.
- [26] H.H. Ou, P.J. Yang, L.H. Lin, A. Masakazu, X.C. Wang, Carbon nitride aerogels for the photoredox conversion of water, Angew. Chem. Int. Ed. 56 (2017) 10905–10910.
- [27] W. Cui, J.Y. Li, W.L. Cen, Y.J. Sun, S.C. Lee, F. Dong, Steering the interlayer energy barrier and charge flow via bioriented transportation channels in g-C<sub>3</sub>N<sub>4</sub>: enhanced photocatalysis and reaction mechanism, J. Catal. 352 (2017) 351–360.
- [28] Y. Zheng, Z.H. Yu, H.H. Ou, M.A. Abdullah, Y.L. Chen, X.C. Wang, Black phosphorus and polymeric carbon nitride heterostructure for photoinduced molecular oxygen activation, Adv. Funct. Mater. 28 (2018) 1705407–1705416.
- [29] J.Y. Li, W. Cui, Y.J. Sun, Y.H. Chu, W.L. Cen, F. Dong, Directional electron delivery via a vertical channel between g-C<sub>3</sub>N<sub>4</sub> layers promotes photocatalytic efficiency, J. Mater. Chem. A 5 (2017) 9358–9364.
- [30] Y.N. Ma, J. Li, E.Z. Liu, J. Wan, X.Y. Hu, J. Fan, High efficiency for H<sub>2</sub> evolution and NO removal over the Ag nanoparticles bridged g-C<sub>3</sub>N<sub>4</sub> and WS<sub>2</sub> heterojunction photocatalysts, Appl. Catal. B: Environ. 219 (2017) 467–478.
- [31] X. Li, J.G. Yu, M. Jarniec, Hierarchical photocatalysts, Chem. Soc. Rev. 45 (2016) 2603–2636.
- [32] X.J. Zou, Y.Y. Dong, S.J. Li, J. Ke, Y.B. Cui, Facile anion exchange to construct uniform AgX (X = Cl, Br, I)/Ag<sub>2</sub>CrO<sub>4</sub> NR hybrids for efficient visible light driven photocatalytic activity, Solar Energy 169 (2018) 392–400.
- [33] X.J. Zou, Y.Y. Dong, S.J. Li, J. Ke, Y.B. Cui, X.X. Ou, Fabrication of V<sub>2</sub>O<sub>5</sub> /g-C<sub>3</sub>N<sub>4</sub> heterojunction composites and its enhanced visible light photocatalytic performance for degradation of gaseous ortho-dichlorobenzene, J. Taiwan Inst. Chem. Eng. 93 (2018) 158–165.
- [34] H. Wang, X. Sun, D. Li, X. Zhang, S. Chen, W. Shao, Y. Tian, Y. Xie, Boosting hot-electron generation: exciton dissociation at the order-disorder interfaces in polymeric photocatalysts, J. Am. Chem. Soc. 139 (2017) 2468–2473.
- [35] X.J. Zou, Y.Y. Dong, C.Y. Yuan, H. Ge, J. Ke, Y.B. Cui, Zn<sub>2</sub>SnO<sub>4</sub> QDs decorated Bi<sub>2</sub>WO<sub>6</sub> nanoplates for improved visible-light-driven photocatalytic removal of gaseous contaminants, J. Taiwan Inst. Chem. Eng. 96 (2019) 390–399.
- [36] Y. Hou, F. Zou, A. Dagg, P.Y. Feng, A three-dimensional branched cobalt-doped α-Fe<sub>2</sub>O<sub>3</sub> nanorod/MgFe<sub>2</sub>O<sub>4</sub> heterojunction array as a flexible photoanode for efficient photoelectrochemical water oxidation, Angew. Chem. Int. Ed. 51 (2013) 1248–1252.
- [37] L. Xiao, S.W. Liu, K. Fan, Z.Q. Liu, B. Song, J.G. Yu, MOF-Based transparent passivation layer modified ZnO nanorod arrays for enhanced photo-electrochemical water splitting, Adv. Energy Mater. (2018) 1800101.
- [38] X.Y. Liu, M. Ye, S.P. Zhang, G.C. Huang, C.H. Li, Y.J. Guo, P.K. Wong, S.W. Liu, Enhanced photocatalytic CO<sub>2</sub> valorization over TiO<sub>2</sub> hollow microspheres by synergistic surface tailoring and Au decoration, J. Mater. Chem. A 6 (2018) 24245–24255.
- [39] C.S. Pan, J. Xu, Y.J. Wang, D. Li, Y.F. Zhu, Dramatic activity of C<sub>3</sub>N<sub>4</sub>/BiPO<sub>4</sub> photocatalyst with core/shell structure formed by self-assembly, Adv. Funct. Mater. 22 (2012) 1518–1524.
- [40] W. Cui, J.Y. Li, F. Dong, Y.J. Sun, G.M. Jiang, W.L. Cen, S.C. Lee, Z.B. Wu, Highly efficient performance and conversion pathway of photocatalytic NO oxidation on SrO-Clusters@Amorphous carbon nitride, Environ. Sci. Technol. 51 (2017) 10682–10690.
- [41] J.Y. Li, X.A. Dong, Y.J. Sun, G.M. Jiang, Y.H. Chu, S.C. Lee, F. Dong, Tailoring the rate-determining step in photocatalysis via localized excess electrons for efficient and safe air cleaning, Appl. Catal. B: Environ. 239 (2018) 187–195.